Received: 7 May 2023 | Revised: 14 August 2023 | Accepted: 7 September 2023

DOI: 10.1002/prot.26594

RESEARCH ARTICLE

PROTEINS WILEY

Structure–function relationships in ShKT domain peptides: ShKT-Ts1 from the sea anemone *Telmatactis stephensoni*

Karoline Sanches[1,2] | Lauren M. Ashwood[3] | Abisola Ave-Maria Olushola-Siedoks[1] | Dorothy C. C. Wai[1] | Arfatur Rahman[1] | Kashmala Shakeel[4] | Muhammad Umair Naseem[4] | Gyorgy Panyi[4] | Peter J. Prentis[3,5] | Raymond S. Norton[1,2]

[1]Medicinal Chemistry, Monash Institute of Pharmaceutical Sciences, Monash University, Parkville, Victoria, Australia

[2]ARC Centre for Fragment-Based Design, Monash University, Parkville, Victoria, Australia

[3]School of Biology and Environmental Science, Faculty of Science, Queensland University of Technology, Brisbane, Queensland, Australia

[4]Department of Biophysics and Cell Biology, Faculty of Medicine, University of Debrecen, Debrecen, Hungary

[5]Centre for Agriculture and the Bioeconomy, Queensland University of Technology, Brisbane, Queensland, Australia

Correspondence
Raymond S. Norton, Medicinal Chemistry, Monash Institute of Pharmaceutical Sciences, Monash University, 381 Royal Parade, Parkville, VIC 3052, Australia.
Email: ray.norton@monash.edu

Present address
Lauren M. Ashwood, QIMR Berghofer Medical Research Institute, Brisbane, Queensland, Australia.

Funding information
Australian Research Council, Grant/Award Number: IC180100021; Hungarian National Research, Development and Innovation Office, Grant/Award Number: K143071; Stipendium Hungaricum Scholarships; Richter Gedeon Talentum Foundation

Abstract

Diverse structural scaffolds have been described in peptides from sea anemones, with the ShKT domain being a common scaffold first identified in ShK toxin from *Stichodactyla helianthus*. ShK is a potent blocker of voltage-gated potassium channels (K_V1.x), and an analog, ShK-186 (dalazatide), has completed Phase 1 clinical trials in plaque psoriasis. The ShKT domain has been found in numerous other species, but only a tiny fraction of ShKT domains has been characterized functionally. Despite adopting the canonical ShK fold, some ShKT peptides from sea anemones inhibit K_V1.x, while others do not. Mutagenesis studies have shown that a Lys–Tyr (KY) dyad plays a key role in K_V1.x blockade, although a cationic residue followed by a hydrophobic residue may also suffice. Nevertheless, ShKT peptides displaying an ShK-like fold and containing a KY dyad do not necessarily block potassium channels, so additional criteria are needed to determine whether new ShKT peptides might show activity against potassium channels. In this study, we used a combination of NMR and molecular dynamics (MD) simulations to assess the potential activity of a new ShKT peptide. We determined the structure of ShKT-Ts1, from the sea anemone *Telmatactis stephensoni*, examined its tissue localization, and investigated its activity against a range of ion channels. As ShKT-Ts1 showed no activity against K_V1.x channels, we used MD simulations to investigate whether solvent exposure of the dyad residues may be informative in rationalizing and potentially predicting the ability of ShKT peptides to block K_V1.x channels. We show that either a buried dyad that does not become exposed during MD simulations, or a partially exposed dyad that becomes buried during MD simulations, correlates with weak or absent activity against K_V1.x channels. Therefore, structure determination coupled with MD simulations, may be used to predict whether new sequences belonging to the ShKT family may act as potassium channel blockers.

KEYWORDS
molecular dynamics, NMR, peptide, potassium channel, sea anemone, ShKT domain, structure determination

1 | INTRODUCTION

The venoms of sea anemones are complex mixtures of biologically active compounds, including peptides, proteins, and low-molecular weight molecules.[1–4] Peptides from the venom of sea anemones, as well as from other parts of these animals,[5] exhibit exceptional molecular diversity, with more than 17 structural scaffolds described,[3,6,7] and more being discovered.[8] A commonly detected scaffold is the ShKT domain, which was first identified in ShK toxin, from the Caribbean sea anemone *Stichodactyla helianthus*.[9] This peptide was isolated on the basis of its activity against potassium channels,[9] and subsequent studies showed that it was a picomolar blocker of the voltage-gated potassium channel $K_V1.3$, but also blocked $K_V1.1$, $K_V1.4$, and $K_V1.6$ at subnanomolar concentrations.[10] As $K_V1.3$ is upregulated in many autoimmune and neuroinflammatory diseases,[11,12] inhibitors of this channel are potentially valuable molecular tools and therapeutic leads; accordingly, selective inhibitors of ShK were developed,[13–16] and one of them, ShK-186 (now known as dalazatide), has successfully completed Phase 1 clinical trials in plaque psoriasis.[17]

Since its discovery in a sea anemone, the ShKT domain has been found in numerous other species, including plants, algae, protozoa, other cnidarians (such as hydra and jellyfish), sea urchins, mollusks, sea squirts, fish, nematodes, parasitic worms, snakes, amphibians, birds, and mammals.[18,19] Indeed, a recent search of the UniProt database[20] identified more than 17 600 ShKT domains, whereas 13 829 ShKT domains in 7329 proteins were found in the SMART nrdb database.[21] These occur as individual peptides (like ShK), repeat sequences containing multiple ShK domains, and ShK domains linked to proteases.[18,22] A recent analysis of the chemical and sequence space of the ShKT superfamily clearly distinguished ShKT domains in the cysteine-rich domains of cysteine-rich secretory proteins (CRISPs) from individual ShKT peptides.[22] Four CRISP subclusters separate out into the main phyla of mammal, insects, and reptiles, whereas ShKT peptides fall into seven subclusters, the largest of which contains members from across the eukaryotes, with a continuum of intermediate properties. Smaller subclusters contained specialized members such as nematode ShK-like sequences, but several subclusters contained no functionally characterized sequences.[22] Indeed, only a tiny fraction of these ShKT domains has been characterized functionally. Several inhibit voltage-gated potassium channels,[18,19,23–26] although some do not,[27,28] even though they adopt the canonical ShK fold.[29] Intriguingly, none of these ShKT peptides from sea anemones has proven to be as potent a blocker of $K_V1.3$ as ShK itself.[10]

A clue to the potentially diverse functions of ShKT domains comes from studies of the model sea anemone *Nematostella vectensis*, which revealed the recruitment of an ShKT domain from the nervous system to venom.[30] This sea anemone produces ShK-like1, which is lethal to fish larvae and found in nematocysts, the venom-producing stinging capsules, as well as ShK-like2, a neuropeptide localized to neurons and involved in development. It was concluded that these two peptides originated from duplication of a ShK-like2 ancestor, a neuropeptide-encoding gene, followed by diversification and partial functional specialization.[30] Thus, it is likely that some ShKT domains from sea anemones and other species may have endogenous neuroendocrine functions.

Numerous genomic, transcriptomic, and proteomic studies of sea anemones have been reported recently.[7,31–35] These studies further highlight, among other findings, the abundance of ShKT domains in sea anemones, and thus the importance of characterizing their function(s). One potential indicator of activity against voltage-gated potassium channels is the presence of a KY (Lys–Tyr) dyad in the sequence, where the Lys and Tyr side chains are in close spatial proximity, as first noted by Ménez et al.[25] Subsequently, it has been recognized that the function of the Tyr residue can be served by a Phe or even a long aliphatic side chain. However, the presence of a KY dyad does not guarantee that an ShK-like peptide will block voltage-gated potassium channels, as illustrated by the peptide OspTx2b, which contains the dyad but failed to show activity against a range of voltage-gated potassium channels expressed in *Xenopus* oocytes or human T lymphocytes.[28] Given the abundance of ShKT domains in nature and the importance of defining their functions, we have investigated whether a combination of structure determination and/or prediction with molecular dynamics (MD) simulations might be useful, at least for predicting activity against voltage-gated potassium channels. The advent of AlphaFold has significantly enhanced the accuracy of peptide and protein structure predictions,[36] especially when homologous structures are available, as in the case of ShKT. However, even disulfide-rich structures such as ShK can exhibit significant conformational dynamics,[37–40] and these dynamics can influence the relative orientation of functionally important side chains.[40,41] We therefore believe that a combination of structure determination and/or prediction with MD simulations is necessary to assess the potential for Kv1.x inhibition. In this study, we have applied this approach to a new ShKT peptide, ShKT-Ts1, from the Australian sea anemone *Telmatactis stephensoni*, a reef-based sea anemone that has caused medically significant human envenomations.[33,42]

2 | MATERIALS AND METHODS

The ShKT-Ts1 sequence was identified in transcriptomic (*e*-value < $1 \times E^{-5}$) and proteomic analyses of the sea anemone *Telmatactis stephensoni*.[33] Gene expression of the ShKT-Ts1 peptide was quantified across six anatomically distinct morphological structures (club-tips, tentacles, actinopharynx, body column, mesenterial filaments, and pedal disc), based on a previously published global

RNASeq dataset.[33] Mass spectrometry imaging (MSI) was utilized to determine the spatial distribution of the ShKT-Ts1 peptide using the methodology described by Surm et al.,[43] with spectra of interest investigated using SCiLS Lab.

2.1 | Recombinant expression of ShKT-Ts1 in *Escherichia coli*

The plasmid vector (pET32a) construct encoding thioredoxin (Trx) followed by a His_6-tag, a tobacco etch virus (TEV) cleavage site, and the ShKT-Ts1 nucleoside sequence, was purchased from GenScript (Piscataway, USA). *E. coli* BL21(DE3) competent cells containing the ShKT-Ts1 vector were grown overnight at 37°C in Luria–Bertani (LB) medium containing 100 mg/mL ampicillin. The overnight culture (1%) was transferred to 1 L LB containing 100 mg/mL ampicillin and incubated at 37°C with agitation at 150 rpm until the optical density at 600 nm (OD_{600}) reached 0.9. The temperature was reduced to 18°C for 1 h, followed by addition of isopropyl-β-D-thiogalactoside (IPTG, Astral Scientific) to a final concentration of 0.5 mM. The culture was incubated overnight at 18°C with agitation at 150 rpm. The samples before and after induction were analyzed by sodium dodecyl sulfate-polyacrylamide gel electrophoresis (SDS-PAGE). The cells were harvested by centrifugation at 5000 g for 15 min at 4°C, and the pellet resuspended in binding buffer (50 mM Tris, pH 8, 500 mM NaCl, 10 mM imidazole) with 1× cOmplete EDTA free protease inhibitor. Cell lysis was achieved by sonication for 3 cycles (30 s on and 30 s off) in ice. The lysate was clarified by centrifugation at 10 000 g for 30 min at 4°C.

2.2 | Isotopic labeling of ShKT-Ts1

Escherichia coli BL21(DE3) competent cells containing the ShKT-Ts1-expression vector were grown overnight at 37°C in LB medium containing 100 mg/mL ampicillin. The overnight culture (1%) was transferred to 4 L LB with 100 mg/mL ampicillin and incubated at 37°C with agitation at 150 rpm until the OD600 reached 0.9. The cells were harvested by centrifugation at 5000 g for 20 min at 20°C and the pellets resuspended in 2 L M9 salts solution.[44] The cells were harvested at 5000 g for 20 min at 20°C and the pellet resuspended in 1 L labeled minimal growth media enriched with 1 g/L $^{15}NH_4Cl$ (Sigma Aldrich). The cells were incubated at 150 rpm at 37°C for 1 h and expression induced with 0.5 mM IPTG at room temperature for 18 h with agitation at 150 rpm. The cells were harvested by centrifugation at 5000 g for 15 min at 4°C, and the pellet resuspended in binding buffer (50 mM Tris, pH 8, 500 mM NaCl, 10 mM imidazole) with 1× cOmplete EDTA free protease inhibitor. Cell lysis was achieved by sonication for three cycles (30 s on and 30 s off) in ice. The lysate was clarified by centrifugation at 10 000 g for 30 min at 4°C.

2.3 | ShKT-Ts1 thioredoxin fusion purification

A metal-chelating affinity column (5 mL Ni Sepharose, GE Healthcare, USA) charged with $NiSO_4$ and pre-equilibrated with binding buffer (10 mM imidazole) was used to purify the ShKT-Ts1 thioredoxin fusion protein. The clarified cell lysate was incubated with the affinity resin at 4°C for 1 h to allow the His-tag to bind. The column was then washed with binding buffer and increasing concentrations of imidazole (20, 40, 60, and 80 mM) to eliminate contaminants. The ShKT-Ts1 thioredoxin fusion was eluted with 100 and 200 mM imidazole, and the eluted fractions analyzed by SDS-PAGE.

2.4 | Buffer exchange and TEV cleavage

Imidazole in the ShKT-Ts1 thioredoxin fusion sample was removed and the sample buffer concurrently exchanged to 50 mM Tris pH 7, 100 mM NaCl, using a 3 kDa Amicon® Ultra-15 centrifugal filter and centrifugation at 3000 g at 4°C. The ShKT-Ts1 thioredoxin fusion was then incubated at 32°C for 3 h with in-house His-tagged TEV protease in 3 mM reduced glutathione (GSH) and 0.3 mM oxidized glutathione (GSSG); this cleavage leaves an additional Gly residue at the N-terminus, which is designated Gly-1 to distinguish it from the native N-terminal residue Ala1. The TEV-treated sample was loaded onto the $NiSO_4$ column prewashed with 50 mM Tris pH 7 containing 100 mM NaCl, and the flow-through was collected. The column was washed with binding buffer (10 mM imidazole) followed by a high concentration of imidazole (1 M) for thioredoxin elution. The flow-through containing the cleaved ShKT-Ts1 was freeze-dried prior to purification on high-performance liquid chromatography (HPLC).

2.5 | High-performance liquid chromatography

The crude peptide was resuspended in 95% solvent A (0.1% trifluoroacetic acid (TFA) in water) and 5% solvent B (0.1% TFA in acetonitrile), filtered with a 0.22 µm syringe filter and loaded onto a C18 reverse-phase (RP-HPLC) column (Vydac, 250 mm × 10 mm, 10 µm, 300 Å) equilibrated in 5% solvent B. An increasing linear gradient of 10%–30% solvent B over 30 min with isocratic flow at 23% B for 5 min was used to elute the peptide, at a flow rate of 4 mL/min throughout.

2.6 | Mass spectrometry

Mass spectrometry was carried out on a Shimadzu LC-MS2020 instrument via a Phenomenex Luna C8 column (100 mm × 2 mm, 3 µm, 100 Å). The gradient for this analysis was from 0% to 80% solvent B at a flow rate of 0.2 mL/min over 20 min.

2.7 | NMR experiments

NMR experiments were performed at 298 K on a Bruker Avance-III 600 MHz spectrometer. Lyophilized ShKT-Ts1 (labeled and nonlabeled) was dissolved in 90% H_2O/10% ^2H_2O at 1 mg/mL (0.3 mM) and the pH was adjusted to 5. The backbone and side chain resonance assignments of ShKT-Ts1 were obtained by analysis of the multidimensional heteronuclear experiments 2D ^1H-^{15}N HSQC, 2D ^1H-^{13}C HSQC (using ^{13}C natural abundance), 3D ^{15}N-edited NOESY-HSQC (mixing time 200 ms) and ^{15}N-TOCSY-HSQC (spin-lock 100 ms).[45] ^1H-^{15}N-HSQC with different ^{15}N spectral widths (35 and 50 ppm) were recorded to identify Arg side chain resonances. Hydrogen-deuterium exchange was monitored by dissolving the lyophilized ShKT-Ts1 in 20 mM deuterated sodium acetate in ^2H_2O at pH 5, and acquiring a series of ^1H 1D and ^1H-^1H 2D TOCSY spectra. The 2D spectra were recorded using 304 and 2048 complex data points in the t_1 and t_2 dimensions, respectively. The 3D spectra were recorded using nonuniform sampling on a 50% Poisson gap sampling schedule[46] for NOESY experiments and 30% for TOCSY, with 200, 64, and 2048 complex data points in the t_1, t_2, and t_3 dimensions, respectively. Spectral reconstruction made use of the iterative soft threshold method (hmsIST).[46] We used NMRpipe[47] to process all the NMR data and CCPNMR analysis[48] for resonance assignments; both were accessed via the NMRbox platform.[49]

2.8 | Structure calculation

Distance restraints for structure calculations were derived from the 3D ^{15}N-NOESY-HSQC and 2D ^1H-^1H NOESY using ARIA 2.1 version 2.3[50,51] in NMRbox.[49] The peptide backbone dihedral angles ϕ and ψ were predicted from chemical shifts using TALOS-N.[52] We recorded a set of hydrogen-deuterium exchange experiments (1D ^1H and 2D ^1H-^1H TOCSY) in 100% ^2H_2O (as described above) to compare the experimental results with the prediction of TALOS-N. Amide hydrogens that exchanged quickly with deuterium (7 min after dissolution in ^2H_2O) were considered to not be involved in ordered secondary structure. Amides that were visible in spectra recorded 12–14 h after dissolution in ^2H_2O were identified as possible hydrogen bond donors involved in secondary structure. Backbone amides that were identified in both TALOS-N and hydrogen-deuterium exchange experiments were included as hydrogen-bond restraints for structure calculations. In the initial structure calculations, we did not include any disulfide bond information as restraints. Based on the proximities of Cys side chains in the structure after these initial calculations, disulfide restraints were then assigned. A final ensemble of 20 structures was generated and analyzed using protein structure validation software.[53]

2.9 | MD simulations

We identified peptides structurally related to the final calculated structure of ShKT-Ts1 using DALI.[54] The four peptides identified were ShK (PDB id 1ROO),[29] BgK (PDB id 1BGK),[25] OspTx2a-p1 (PDB id 6CKD)[24] and MMP23 (PDB id 2 K72).[18] MD simulations were performed using GROMACS version 2021.1,[55] and the Amber99sb[56] force field. Simulations used periodic boundary conditions with cell dimensions 5.56 nm × 5.56 nm × 5.56 nm, with the TIP3P water model. Ions were included to neutralize the net positive charge on the peptides, and the particle-mesh Ewald (PME)[57] method was used for treatment of long-range electrostatic interactions. Simulations were performed at a temperature of 293 K using isotropic pressure coupling with the Parrinello–Rahman[58] and V-rescale thermostat.[59] The starting models were minimized using steepest descents method. Systems were equilibrated under the *NVT* ensemble (constant number of particles *N*, volume *V*, and temperature *T*; 50 ns). Production simulations (1 μs) were run at 1 atm using the *NPT* ensemble.

2.10 | Cytotoxicity

The sulforhodamine B (SRB) assay was undertaken to assess the cytotoxicity of ShK-Ts1 against adherent cells, and was performed according to published protocols.[60,61] Briefly, two macrophage cell lines, RAW 264.7 and immortalized bone marrow-derived macrophages (iBMDM), were seeded at 5 × 10^3 cells/100 μL/well in a 96-well flat-bottom plate, and incubated overnight at 37°C in a humidified incubator with 5% CO_2. Macrophages were then treated with ShKT-Ts1 (10 and 20 μM) for 48 h. To fix cells to the plate, a fixation solution (10% vol/vol trichloroacetic acid) was added directly to the culture media and incubated at 4°C. After 2 h the solution was gently removed and cells were rinsed with water, prior to drying at room temperature. SRB solution (0.2% wt/vol in 1% vol/vol acetic acid) was then added and incubated for 45 min. Unbound dye was removed by acetic acid solution (1% vol/vol). Protein-bound dye was solubilized with 10 mM Tris base (pH 10.5) and absorbance measured at 560 nm using an EnVision (PerkinElmer) plate reader.

2.11 | Mammalian cell cultures and transfection of ion channel genes

Chinese hamster ovary (CHO) cells (ATCC, Germany) were grown in Dulbecco's modified Eagle medium supplemented with 10% fetal bovine serum (FBS), 2 mM L-glutamine, 100 μg/mL streptomycin and 100 U/mL penicillin-g (Sigma-Aldrich, St. Louis, MO) in a humidified incubator at 37°C and 5% CO_2. Cells were passaged every 2–3 days following a 5 min incubation in 0.05% trypsin–EDTA solution.

CHO cells were transiently transfected with plasmids encoding the following ion channels using Lipofectamine 2000 kit (Invitrogen, Waltham, MA) according to the manufacturer's protocol: $hK_V1.1$, $hK_V1.2$, and $hK_V1.6$ in pCMV6-AC-green fluorescent protein (GFP) plasmid (OriGene Technologies, Rockville, MD), $hK_V1.4$ in pCDNA3 plasmid, $hK_V1.5$, in pEYFP-C1 plasmid (a kind gift from A. Felipe, University of Barcelona, Barcelona, Spain), $hK_{Ca}3.1$ in pEGFP-C1 vector (a kind gift from H. Wulff, University of California, Davis, CA) and

hNa$_V$1.5 (a kind gift from H. Abriel, University of Bern, Bern, Switzerland). The cells were cotransfected with a plasmid encoding GFP at a GFP:channel DNA molar ratio of 1:10 for hK$_V$1.4. After 24 h of transfection, GFP-positive cells were identified with Nikon TE 2000 U fluorescence microscope (Nikon, Tokyo, Japan) using bandpass filters of 455–495 and 515–555 nm for excitation and emission, respectively, (>70% success rate for transfection) and currents were recorded. Human embryonic kidney 293 cells stably expressing mK$_{Ca}$1.1 (BKCa, a kind gift from C. Beeton, Baylor College of Medicine, Houston), or hNa$_V$1.4 (a kind gift from P. Lukács, Eötvös Loránd University, Budapest, Hungary) were used. hK$_V$1.3 currents were recorded from activated T cells. To obtain human T cells, mononuclear cells from healthy donors' blood were separated through Histopaque1077 (Sigma-Aldrich, St. Louis, MO) density gradient centrifugation and cultured in Roswell Park Memorial Institute (RPMI) 1640 medium containing 2 mM L-glutamine, 10% FBS, 100 µg/mL streptomycin and 100 U/mL penicillin-g at a density of 5×10^5 cells per mL in a humidified incubator at 37°C and 5% CO_2. Phytohemagglutinin A was also added to the medium at a concentration of 2, 5, and 10 µg/mL to enhance the expression of K^+ channels. Patch-clamp experiments were performed after 3–6 days of activation.

2.12 | Electrophysiology

Whole-cell currents were recorded using conventional patch-clamp electrophysiology following standard protocols.[62] Micropipettes were pulled from Borosilicate Standard Wall with Filament glass (Harvard Apparatus Co., Holliston, MA) in four stages using a Flaming Brown automatic pipette puller (Sutter Instruments, San Rafael, CA), resulting in electrodes having 3–6 MΩ resistance in the bath solution. All measurements were performed at room temperature (20–25°C) using a Multiclamp 700B amplifier connected to a computer with Axon Digidata1440 digitizer. For data acquisition, Clampex 10.7 software was used (Molecular Devices, Sunnyvale, CA). Current records were discarded when the leak current at holding potential (V_h) was >10% of peak current at the test potential.

All salts and components of the solutions were purchased from Sigma Aldrich, St. Louis, MO. The intracellular (pipette) solution (ICS) for recording K$_V$1.x and K$_{Ca}$1.1 currents consisted of (in mM) 140 KF, 2 $MgCl_2$, 1 $CaCl_2$, 11 EGTA, and 10 HEPES. The composition of ICS for Na^+ channels was (in mM) 10 NaCl, 105 CsF, 10 HEPES, 10 EGTA, and for hK$_{Ca}$3.1 channels (in mM) 150 K-Asp, 5 HEPES, 8.5 $CaCl_2$, 2 $MgCl_2$, and 10 EGTA. The pH of ICS was set to 7.22 and osmolarity was ~295 mOsM. The extracellular (bath) solution (ECS) consisted of (in mM) 145 NaCl, 5 KCl, 2.5 $CaCl_2$, 1 $MgCl_2$, 10 HEPES, and 5.5 glucose, pH 7.35 for all the ion channels included in this study. The osmolarity of the ECS was 302–308 mOsM. In the HK-150 and Na^+-free ECS, all Na^+ was substituted by K^+ or choline-Cl, respectively; other ingredients remained unchanged. In the various tetraethylammonium (TEA^+)-containing solutions, Na^+ was substituted by TEA^+-chloride in equimolar concentration. ShKT-Ts1 and positive controls were dissolved in ECS supplemented with 0.1 mg/mL bovine serum albumin. The cells were perfused with control and test solutions using a gravity-driven perfusion system and AutoMate Perfusion Pencil Multi-Barrel Manifold Tip (AutoMate Scientific, Berkeley, CA). Excess ECS was removed continuously by vacuum suction. The complete exchange of solution in the bath chamber, that is, the proper operation of the perfusion apparatus, was confirmed frequently using either fully reversible inhibitors (TEA^+ for K$_V$1.1, K$_V$1.3, K$_V$1.6, and mK$_{Ca}$1.1, charybdotoxin (ChTx) for K$_V$1.2, 4-aminopyridine (4-AP) for K$_V$1.5, and Tram34 for K$_{Ca}$3.1), or ECS (HK-150 for K$_V$1.4 to eliminate the driving force for K^+ during depolarization to 0 mV or Na^+-free solution for Na$_V$ channels) as positive controls.

For recording the currents of K$_V$1.x channels, 15–300 ms long depolarization pulses to +50 mV (except where indicated) were applied from a holding potential (V_h) of −120 mV every 15 s and peak currents were measured. Owing to the highly variable activation kinetics of K$_V$1.2,[63] the pulse duration was set between 15 and 300 ms to maximize open probability of the channel. The slower inactivation rate of K$_V$1.2 prevented inactivation even at 300-ms-long depolarization pulses. mK$_{Ca}$1.1 currents were evoked by depolarizing the cells to +100 mV for 600 ms from a V_h of −100 mV. Test pulses were delivered every 15 s. For K$_{Ca}$3.1 currents, 150-ms-long voltage ramps to +50 mV from −120 mV were applied every 10 s. The V_h was set to −85 mV. For Na$_V$1.x current recordings, 15-ms-long voltage steps from a V_h of −120 to 0 mV were applied every 10 s.

Patch-clamp data were analyzed using pClamp 10.7 software package (Molecular Devices, Sunnyvale, CA) and GraphPad Prism software (version 8.0.1, La Jolla, CA). Whole-cell current traces were digitally filtered with a three points boxcar smoothing filter and were corrected for ohmic leakage when needed. The inhibitory effect of a peptide toxin at a given concentration was calculated as remaining current fraction (RCF = I/I_0, where I_0 is the peak current in the absence of the toxin, and I is the peak current after 3–5 min perfusion by ShKT-Ts1. Peptide concentrations were based on dry weight, without any correction for TFA content.

2.13 | Chemical space analysis

ShKT domain sequence datasets used for the principal component analyses (PCAs) were retrieved from Uniprot.[20] The dataset (ShKT6103) consists of ShKT domains from sea anemones, specifically UniProtKB sequences classified under the ShKT Domain [FT] with Taxon ID 6103 (order Actiniaria). Protein existence was set to include only sequences whose existence was supported by experimental evidence at protein level, transcript level or those inferred from homology; sequences with predicted and uncertain existence were filtered out of the dataset. ShKT domain subsequences (where the ShKT domain is part of a larger sequence) were retained. The dataset was examined for redundancies, and for sequences with multiple ShKT domains, each individual domain was labeled numerically, beginning from the N-terminus. After the inclusion of ShKT-Ts1, the final dataset consisted of 88 ShKT domain sequences. Multiple sequence alignments (MSA) were generated using Clustal Omega,[64] and alignment

columns composed mainly of gaps with a residue consensus lower than 7% were removed. Alignment visualization and editing were carried out in Jalview v2.11.2.6,[65] which defines residue consensus as the commonest residues and is expressed as a percentage for each column of the alignment. The MSAs were fed into the QIIME2[66] plugin for PCA analysis of protein sequence phylogeny, q2-protein-pca pipeline, as described by Wang and Kennedy.[67] The EMPeror software[68] was used for PCA loadings and scores plots visualization.

3 | RESULTS

3.1 | Gene expression and peptide distribution

The transcript corresponding to ShKT-Ts1 was not significantly differentially expressed across the six morphological structures examined (four-fold expression difference, false discovery rate ≤0.05), but a trend toward higher expression was observed in the mesenterial filaments (Figure 1A). MALDI-MSI identified that the abundance of a spectral peak (4206 *m/z*) close to the expected mass of ShKT-Ts1 peptide was greatest in the region corresponding to the mesenterial filaments of *T. stephensoni*, which play a role in digestion and prey killing (Figure 1).

3.2 | Resonance assignments

We expressed ShKT-Ts1 as described in Section 2. The successful expression of ShKT-Ts1 is documented in the SDS-PAGE in Figure S1A. After expression, the peptide-fusion with Trx was purified using nickel affinity with an increasing imidazole gradient (Figure S1A). After TEV cleavage, a second nickel affinity purification was used to separate the cleaved peptide from Trx and TEV (Figure S1A). ShKT-Ts1 was then purified using RP-HPLC (Figure S1B), and the mass and purity of the peptide were confirmed by LCMS, as shown in Figures S2 (unlabeled ShKT-Ts1) and S3 (^{15}N-labeled). The mass determined by LCMS confirmed that the peptide was fully oxidized after cytoplasmic expression and TEV-cleavage, with no extra step necessary for oxidative folding. Note that the recombinant peptide, on which all structural and functional characterization was conducted, contains an additional N-terminal Gly relative to the native ShKT-Ts1 sequence.

We acquired a series of 1D ^{1}H spectra at different pH values and temperatures (Figures S4 and S5, respectively) to identify the best conditions for resonance assignments and structure calculations. The pH titration from 2 to 7 showed that spectra at pH 4 and 5 had better peak dispersion over the amide/aromatic region; pH 5 was chosen as some peaks that are missing or overlapping at other pHs are resolved

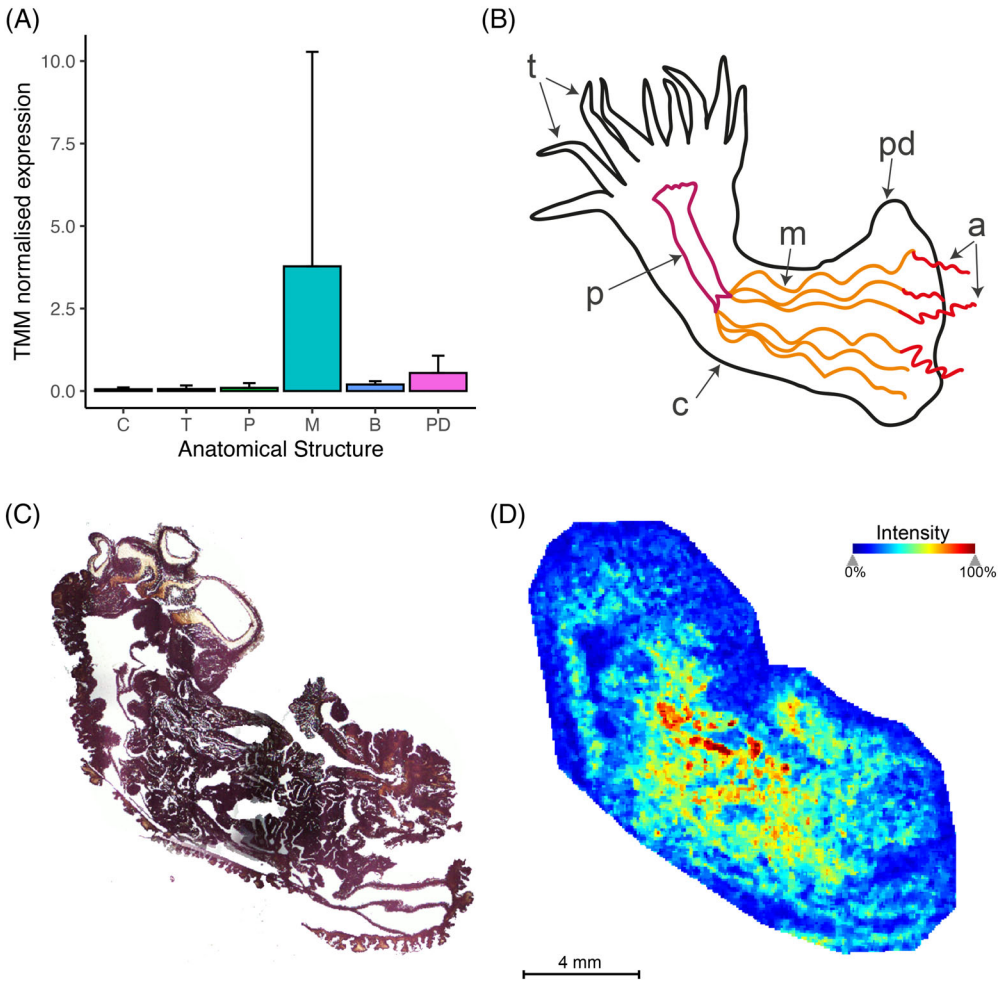

FIGURE 1 Expression patterns and abundance of the ShKT-Ts1 peptide across functional regions in *Telmatactis stephensoni*. (A) Bar graph of ShKT-Ts1 expression patterns. (B) Schematic of the morphological structures sampled. (C) Hematoxylin and eosin-stained longitudinal section of a *T. stephensoni* individual. (D) Mass spectrometry imaging (MSI) data showing the abundance of ShKT-Ts1 in *T. stephensoni*. a, acontia; b, body column; c, club-tips; m, mesenterial filaments; p, pharynx; pd, pedal disc; t, tentacles.

at pH 5 (Figure S4). 1D ^{1}H NMR spectra of ShKT-Ts1 at different temperatures (278–308 K) at pH 5 were also acquired (Figure S5); 298 K was chosen for structure calculation as it shows better peak dispersion through the amide and aromatic region, especially at 7–8 ppm.

ShKT-Ts1 peptide has 36 amino acid residues, with an extra N-terminus Gly following TEV-cleavage (designated Gly-1 to distinguish it from the native N-terminal residue Ala1), making a total of 37 amino acids. The ^{15}N-HSQC (Figure 2) shows 44 peaks because of side chain resonances of Asn4 and Asn5 (Hδ), and Arg9, Arg13, Arg14, and Arg25 (Hε). The folded peak of the Lys31 side chain is also observed at 6.9 ppm on ^{1}H and 106.5 ppm on ^{15}N. A ^{15}N-HSQC with increased ^{15}N spectral width was acquired for identification and assignment of Arg side chain resonances (Figure S6). The chemical shifts of all ^{1}H and ^{15}N resonances are listed in Table S1 in the Supporting information S1, and have been deposited in BioMagResBank[69] with id number 51896.

3.3 | ShKT-Ts1 solution structure

We used 956 NOE distance restraints for calculation of the structure of ShKT-Ts1, where 466 are intra-residue, 231 sequential, 146 medium range ($2 \le |i-j| \le 5$), and 113 long range ($|i-j| > 5$; Table S2). To calculate the initial structures, we used only the NOE restraints and did not specify any disulfide connections. Hydrogen bond restraints were included based on hydrogen-deuterium exchange experiments (Figure S7) and TALOS-N[52] prediction. After convergence of the initial structures, well-defined disulfide connectivities based on the proximity of the cysteines and NOEs between the sidechains were identified and included in further structure calculations. The calculated structures were energetically refined through MD simulations in explicit water using ARIA; the final ensemble of 20 lowest energy structures of ShKT-Ts1 is shown in Figure 3A and deposited in the Protein Data Bank (PDB id 8SED). The structures are well-defined, with backbone (N, C, and Cα) and heavy atom RMSDs for all residues of 0.7 and 1.2 Å, respectively. Table S2 summarizes the structural statistics.

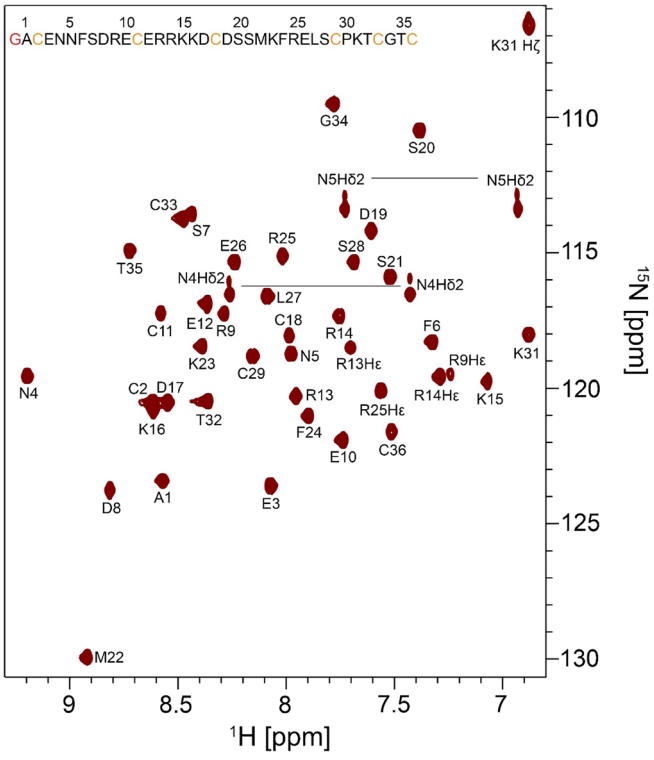

FIGURE 2 ^{1}H-^{15}N-HSQC of ShKT-Ts1 at pH 5 and 298 K. A total of 44 amide peaks was observed, as expected for 37 amino acids with two Asn and four Arg; the folded Lys31 side chain resonance is at 6.9 ppm in the ^{1}H dimension and 106.5 ppm in ^{15}N.

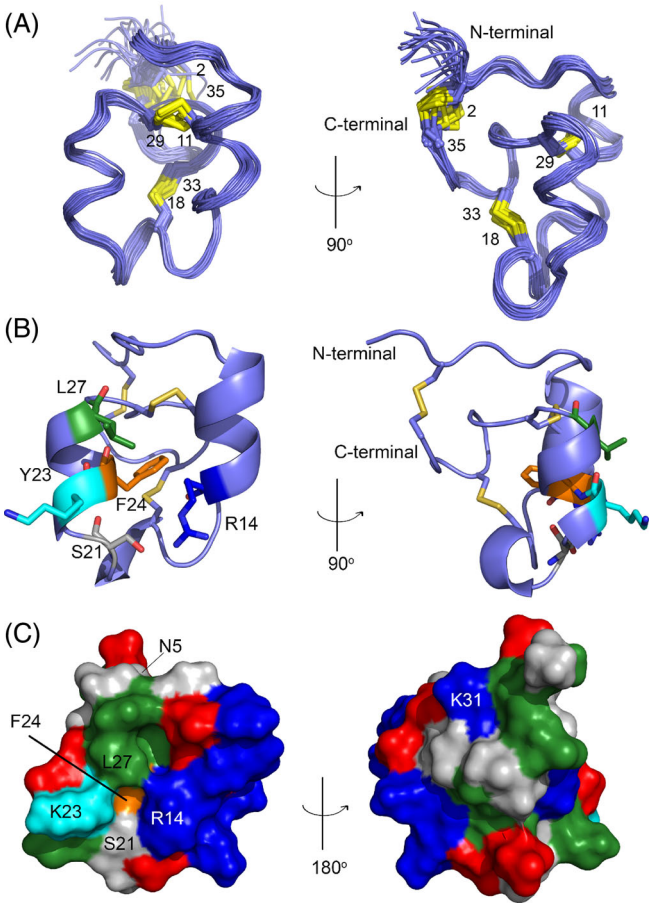

FIGURE 3 ShKT-Ts1 solution structure. (A) The 20 best energy structures of ShKT-Ts1 superimposed over Cα are represented as ribbon (blue). The three disulfide bonds (C2—C35, C11—C29, and C18—C33) are shown as yellow sticks and the numbers indicate each cysteine. (B) Cartoon representation of the best energy ShKT-Ts1 structure. The α-helices are colored in blue. The three disulfide bonds, the Lys23 and Phe24 side chains, and several surrounding residues are shown in stick representation. (C) Surface representation of ShKT-Ts1 showing the negatively charged side chains in red (Asp, Glu), positively charged in blue (Lys, Arg), hydrophobic in green (Ala, Cys, Leu, Met, Phe); all the others (Asn, Ser, Thr, Gly, Pro) are in gray and were identified using the Kyte and Doolittle scale.[73] While Lys23 (cyan) is solvent exposed, Phe24 (orange) is buried, being surrounded by hydrophilic residues Arg14, Ser21, Lys23, and Leu27.

ShKT-Ts1 has the disulfide bond connectivities C1—C6, C2—C4, and C3—C5 (Figure 3B), as in other ShK-like peptides. The Asp/Asn interaction with Lys–Thr is conserved among ShKT domains and has been shown to be important for peptide folding; Asn5 and Lys31 are labeled in Figure 3C.[25,29,70]

Although ShKT-Ts1 has a ShK-like disulfide bond scaffold, its 3D structure shows slight differences from that of ShK. While ShK has two short α-helices encompassing residues 14–19 and 21–24,[29] ShKT-Ts1 has a short 3_{10} helix (18–20) between two α-helices encompassing residues 8–14 and 22–27. The N-terminus adopts an extended conformation up to residue 8. ShKT-Ts1 lacks the critical Lys–Tyr dyad (Lys22–Tyr23 in ShK), but it has a Lys–Phe (Lys23–Phe24) which could perhaps support activity against voltage-gated potassium channels, as previous work has shown the importance of a cationic/hydrophobic residue pair for inhibitory activity.[25] However, while Lys23 in ShKT-Ts1 is solvent-exposed in the structure, Phe24 is buried, shielded by the surrounding hydrophilic residues Arg14, Ser21, and Leu27 (Figure 3C). The location of several charged side chains on the surface of ShKT-Ts1 is highlighted in Figure 3C. While the negatively charged Glu and Asp are distributed throughout the peptide, the positively charged Arg and Lys are mostly concentrated in the α-helix 8–14. Like other disulfide-rich peptides, ShKT-Ts1 lacks a canonical hydrophobic core, and instead the hydrophobic side chains are solvent exposed, or partially exposed, surrounded by hydrophilic side chains, which are organized as surface hydrophobic clusters, as observed in other disulfide-rich peptides.[71,72] Here, the hydrophobic residues were identified using the Kyte and Doolittle scale[73]; the surface representation of ShKT-Ts1 shows that the only hydrophobic residue that is buried is Phe24 (Figure 3C).

3.4 | Cytotoxicity

We investigated the cytotoxicity of ShKT-Ts1 using the SRB assay. The assay was performed 48 h after ShKT-Ts1 treatment and showed that the relative cell densities in wells treated with 10 μM peptide were > 99% of untreated control for both RAW 264.7 (Figure S8A) and iBMDMs (Figure S8B). Cell densities with 20 μM peptide treatment were > 97% of untreated control for RAW 264.7 and >99% for iBMDMs, indicating that high concentrations of ShKT-Ts1 did not affect macrophage proliferation.

3.5 | Ion channel activity

The typical functional Lys–Tyr dyad found in ShK peptide is present as Lys–Phe in ShKT-Ts1, suggesting that it may block voltage-gated K^+ channels. Therefore, we tested the effect of 100 nM recombinant ShKT-Ts1 on the first six members of human K_V1 channel family, $hK_V1.1$–$hK_V1.6$ (Figure S9A–G) as a standard K_V panel established in our laboratory.[74] To test whether these channels were inhibited by ShK-Ts1, we first recorded whole-cell currents in control conditions, and then the operation of the microperfusion system was confirmed using reversible blockers of the respective channels (Figure S9A–C,F,G) or HK-150 solution for $hK_V1.4$ (Figure S9E). In the latter case, in the absence of a reversible blocker for $hK_V1.4$, the full solution exchange was confirmed by ~0 K^+ current in symmetric K^+ concentrations and at 0 mV test potential (Figure S9E). Having confirmed proper solution exchange, the recombinant peptide at 100 nM concentration was applied and the whole-cell currents were recorded for 12–20 consecutive depolarizing pulses in the presence of ShK-Ts1 corresponding to 3–5 min exposure. None of the $hK_V1.x$ currents was inhibited by 100 nM ShK-Ts1 under these conditions (Figure S9A–G, L). We then extended our study to other channels: $mK_{Ca}1.1$, the large conductance voltage- and Ca^{2+}-activated channel (Figure S9H); $hK_{Ca}3.1$, a Ca^{2+}-activated K^+ channel (Figure S9I); and two human voltage-gated Na^+ channels $hNa_V1.4$ (Figure S9J) and $hNa_V1.5$ (Figure S9K). We found that 100 nM ShKT-Ts1 did not inhibit any of the channels investigated in this study (Figure S9L).

3.6 | Chemical space analysis

Previously, Shafee et al.[22] had illustrated the utility of chemical/sequence space analysis to cluster sequences within the ShKT superfamily based on their biophysical properties. This analysis clearly distinguished ShK-like peptides from the cysteine-rich domains of CRISPs, but also demonstrated subclustering within the superfamily and provided some insight into the taxonomic and functional properties of sequences within the ShKT clusters. We have used a similar approach to determine whether PCA could shed light on the lack of ion channel activity of ShKT-Ts1. The PCA loadings plot (Figure S10A) describes the level of conservation at each alignment position; the dots represent the PC1 and PC2 loadings of each position and are an indication of the level of influence of each position. Along the PC1 and PC2 axes, it can be inferred that the alignment positions 8, 20, 7, and 19, corresponding to ShK Arg11 and Ser10 (alignment positions 20 and 19 are gaps) are most influential in driving the direction and distance of sequence separation in the PCA scores plot, as these have the largest absolute PCA loadings values. The alignment position 5 (ShK Pro8) has a significant influence along the PC2 axes.

The PCA scores plot of the ShKT6103 dataset revealed the close spatial positioning of similar sequences in PCA space and suggested that the analysis may be useful in relating the spread of sequences within a sequence group to sequence homology (Figure S10). However, no consistent function-based clustering was apparent, as evidenced from the significant separation in space between OspTx2b and AsK132958, which are peptides that have shown no activity against a range of $K_v1.x$ isoforms, and the proximity of OspTx2a, which has weak $K_V1.x$-inhibitory activity, to OspTx2b, which showed no activity. ShKT-Ts1 is relatively close to ShK and yet their $K_V1.x$-inhibitory activities are starkly different (Figure S10B). In contrast, ShK and BgK, both of which are potent blockers of $K_V1.x$ channels, are not close to one another, although ShK is close to HmK, which is a potent blocker (Figure S10B). In order for analyses such as this to be useful as predictors of function, a more specific clustering based on a

group of residues that have been shown to be important in channel binding in ShK (beyond just the KY dyad) would be worth exploring.

3.7 | MD simulations of ShKT-Ts1 and structurally related peptides

We have previously noted that even small disulfide-rich peptide toxins display dynamics that may be important for molecular recognition,[40,41] and a combination of NMR relaxation and high-pressure NMR measurements confirmed that ShK samples conformations in which the dyad residues may be more exposed to solvent.[37–39] ShKT-Ts1 has a Lys23–Phe24 sequence that could play a role in blocking potassium channels, as previous work has shown the importance of a cationic/hydrophobic residue pair for this activity.[25] However, the 3D structure of ShKT-Ts1 showed that Phe24 is largely buried and protected from solvent by the surrounding hydrophilic residues Arg14, Ser21, and Lys23, as shown in Figure 3C.

We employed MD simulations of ShKT-Ts1 over 1 μs to investigate the presence of conformational dynamics in ShKT-Ts1 that may modify the solvent exposure of Phe24. To understand the fundamental motions of ShKT-Ts1, we employed PCA (also known as essential dynamics analysis)[75] over the 1 μs trajectory. We extracted the atomic positions of all atoms from the MD trajectories and built a covariance matrix, where the diagonalization provides a set of eigenvectors and associated eigenvalues that represent the principal motion directions of the peptide. The 20 representative structures over the first and second principal components (PC1 and PC2) were extracted, overlaid on the Cα atoms, and colored as rainbows, as shown in Figure 4A. This analysis identified the region comprising the helix 3_{10} as being involved in conformational changes, leading to an untwisted conformation of the region from Arg15 to Lys23, which brings the side chains of Glu26 Oε and Arg14 Nη as close as 4 Å (Figure 4B). These salt bridges stabilize the folding of ShKT-Ts1 and contribute to Phe24 being shielded from solvent (Figure 4B). To assess the exposure of the dyad, we calculated the solvent-accessible surface area (SASA) for each residue over the 1 μs trajectory. The average SASA indicates that Lys23 is more exposed to solvent than Phe24 in ShKT-Ts1 (Figure S11). The comparison between the SASA of the NMR solution structure and the AlphaFold-predicted structure indicates that the exposure for both Lys23 and Phe24 is overestimated in the predicted structure.[76]

The observation that Phe24 is buried in the calculated structures, and largely remains so during the MD simulations, could be a significant contributor to the lack of activity of ShKT-Ts1 against K_V1.x channels. In contrast, ShK,[9,29] which shows an overall 3D fold similar to ShKT-Ts1 (Figure 5A,B), blocks K_V1.3 with 11 pM[10] and has the dyad Lys22–Tyr23 exposed to the solvent and thus available for interactions with the pore of the channel (Figure S11).[41]

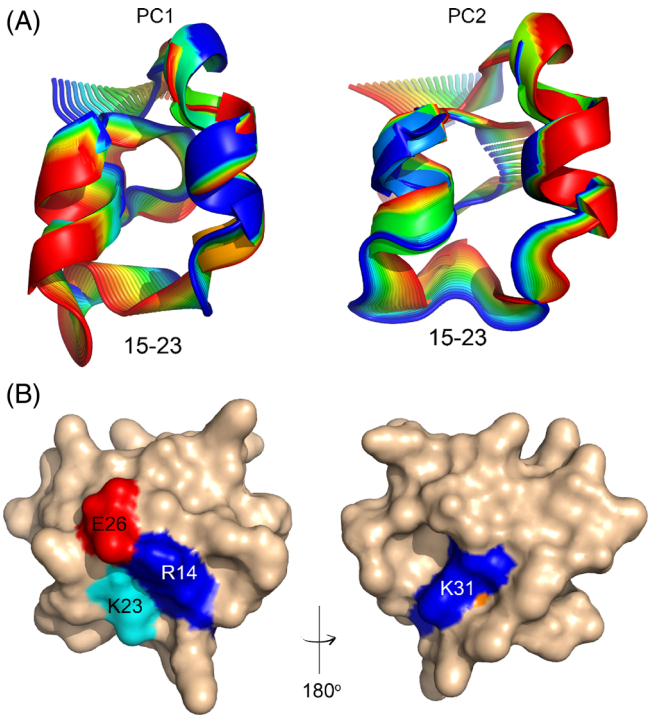

FIGURE 4 MD simulations of ShKT-Ts1. (A) PCA analysis show higher dynamics in the region encompassing Arg15–Lys23. (B) Average structure over 1 μs trajectory represented as a surface. Lys23 is shown in cyan, Arg15 and Lys31 in blue, and Glu26 in red. Phe24 is colored in orange and is largely buried by electrostatic interactions formed by Glu26–Arg14 side chains and the Lys31 Nζ side chain and backbone carbonyl of Arg14.

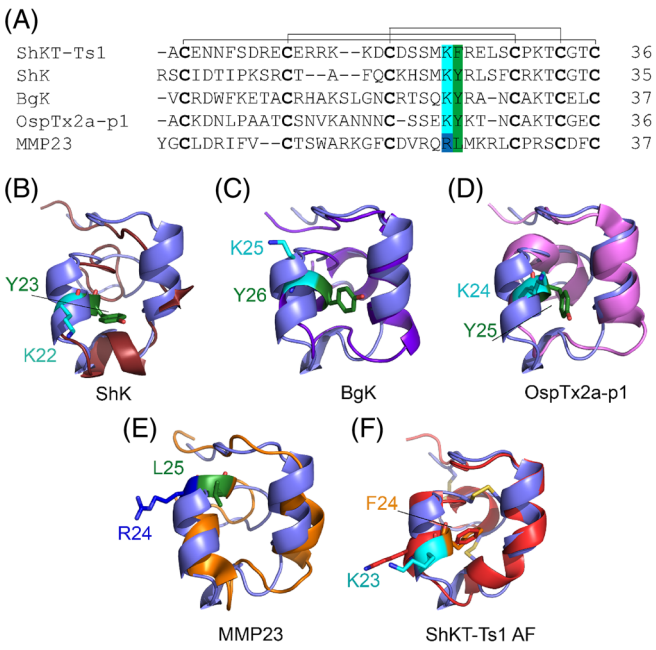

FIGURE 5 Comparison between the solution structure of ShKT-Ts1 determined here (blue) and structurally related ShKT peptides. (A) Sequence alignment (performed using Clustal Omega[64]) showing the dyad Lys–Tyr/Phe/Leu in cyan and green, respectively. (B) ShKT-Ts1 as cartoon representation (blue) and ShK (PDB id 1ROO) in dark red.[29] Lys and Tyr dyad residues are shown as sticks (cyan and green, respectively). (C) BgK (PDB id 1BGK)[25] in purple. (D) OspTx2a-p1 (PDB id 6CKD)[24] in pink. (E) MMP23 (PDB id 2K72)[18] in orange. (F) The AlphaFold2 predicted structure of ShKT-Ts1 in red, including the side chains of Lys23 and Phe 24. Lys23 and Phe24 in the solution structure are shown in cyan and orange, respectively.

We used in silico calculations to extend our studies of conformational changes in other peptides structurally related to ShKT-Ts1. Those peptides, identified by DALI,[54] are the sea anemones toxins[29] BgK (PDB id 1BGK),[25] and OspTx2a-p1b (PDB id: 6CKD),[24] as well as MMP23 (PDB id 2K72),[18] which is a metalloprotease with an ShK-like domain (Figure 5). The sequence alignment of these peptides shows conserved disulfide bonds and the dyad formed by Lys (or Arg in the case of MMP23, although there is a nearby Lys that may serve this function) followed by a hydrophobic amino acid (most of them aromatic, except for MMP23 where it is Leu; Figure 5A).

BgK[25,77] (Figure 5C) blocks $K_V1.3$ with *Ki* 0.7 nM, whereas OspTx2a-p1 (Figure 5D) is a weak inhibitor of $K_V1.2$ and $K_V1.6$ channels.[24] MMP23 contains a ShKT domain that displays three short α-helices encompassing residues 10–14, 23–29, and 31–34[18] (Figure 5E). Figure 5F compares the lowest-energy solution structure of ShKT-Ts1 determined in this study with the structure predicted by AlphaFold.[36] Although there is good agreement between the experimental and predicted structures, the predicted structure shows a more exposed dyad than the experimental structure. As discussed below, the solvent exposure of Lys23–Phe24 in the predicted structure does not correlate with the lack of activity on potassium channels.

The calculated average SASA for the AlphaFold structure also confirms that the dyad is more exposed than in the experimental NMR structure. In the case of ShK, both Lys and Tyr are the most exposed dyad compared with other sea anemone peptides (Figure S11). Over the course of the MD simulations, we performed PCA analysis and extracted the first PC for each peptide, which shows conformational dynamics that result in varying solvent exposure of the dyad, as summarized in Figure 6. In ShKT-Ts1, a conformational change in the 3_{10} helix and surrounding residues (from 15 to 23) brings Arg14 close to Glu26, as a result of which Phe24 becomes fully buried. BgK and MMP23 also have the dyad exposed to the solvent and are both relatively rigid throughout the trajectory (Figure 6). Interestingly, the peptides with the dyad exposed (ShK and BgK) showed activity against $K_V1.x$ channels. ShK blocks $K_V1.3$ with 11 pM,[10] while

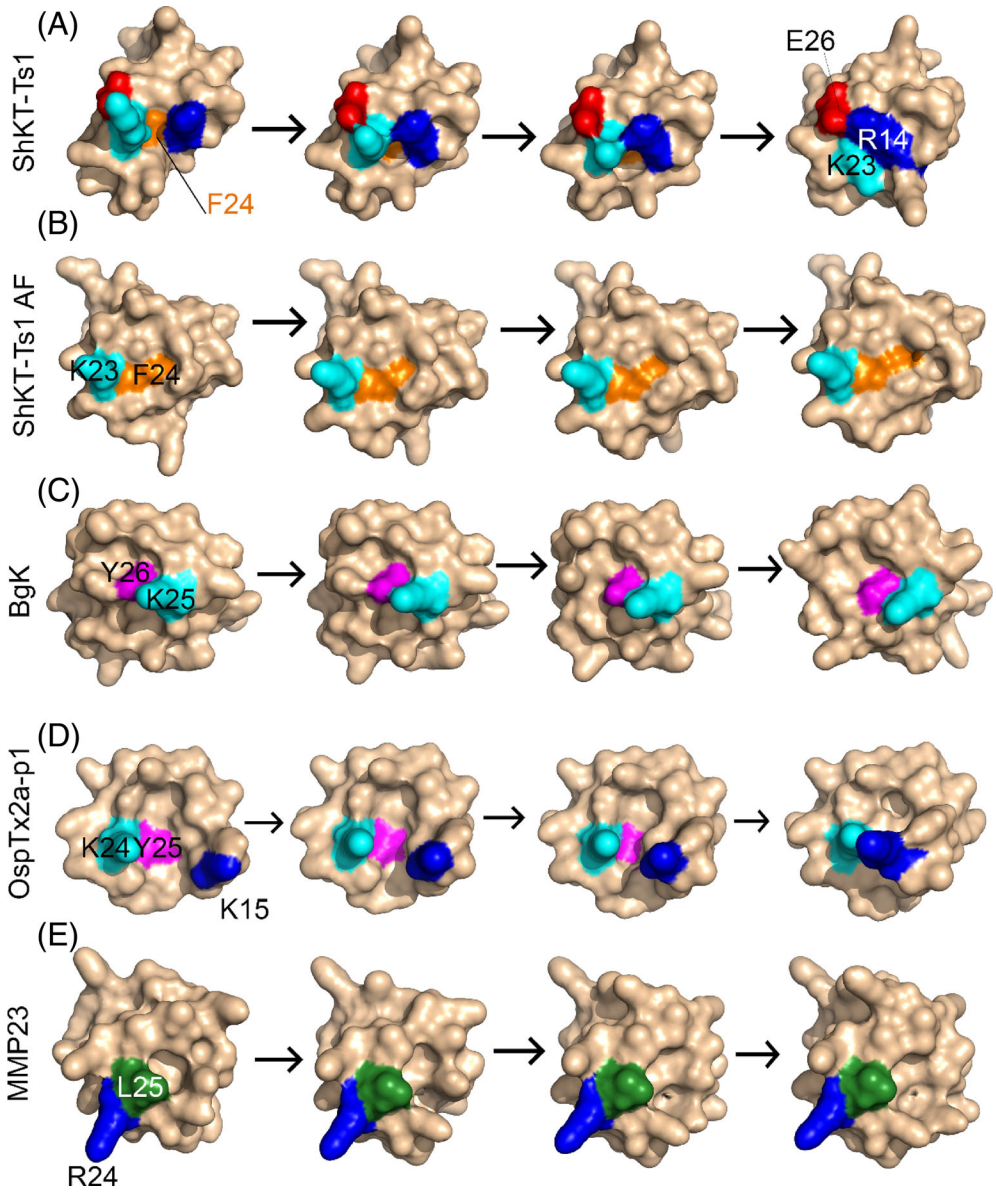

FIGURE 6 Four representative structures over the first principal component (PC1) over the course of a 1 μs MD trajectory for four ShKT family peptides, represented as surfaces (colored wheat). The dyad for each one is cyan for Lys, magenta for Tyr, or orange for Phe, as shown for ShKT-Ts1 (dyad Lys23–Phe24). (A) ShKT-Ts1 NMR. (B) The structure for ShKT-Ts1 predicted by AlphaFold.[36] (C) BgK (Lys25–Tyr26).[25] (D) OspTx2a-p1 (Lys24–Tyr25).[24] (E) The dyad in MMP23[18] is composed of Arg24 and Leu25, which are colored blue and green, respectively.

BgK blocks a range of K_V1.x channels with nM affinities.[25,78] OspTx2a-p1, which blocks K_V1.2 and K_V1.6 channel currents at low μM concentrations,[24] has a partially exposed Tyr25 in a pocket that is completely buried when conformational changes bring Arg15 close to Lys24 (Figure 6), probably also involving a rearrangement with the water. We propose a relationship between the static exposure of the dyad, the effects of local structural dynamics on that exposure, and the activity against K_V1.x channels, where peptides with the dyad exposed can bind to the pore of the channel. Although the dyad is exposed in MMP23, it is not a Lys–Tyr as found in K_V blockers, but instead Arg–Leu, which may contribute to the low potency against K_V1.3 (~3 μM).[18]

As indicated above, the structure of ShKT-Ts1 predicted by AlphaFold is very similar to the experimentally determined solution structure. It has been noted, however, that AlphaFold structures are likely to be less reliable in regions with conformational dynamics and to have more hydrogens bonds than those observable by NMR.[76] We therefore subjected the structure of ShKT-Ts1 predicted by AlphaFold to the same MD simulations. As shown in Figure 6B, the Lys23–Phe24 dyad remains solvent-exposed throughout the simulation, in contrast to the solution structure, where it is partially buried to begin with and becomes fully buried during the simulation.

4 | DISCUSSION

In this study, we determined the structure of ShKT-Ts1, a new peptide from the sea anemone *Telmatactis stephensoni*, and examined its tissue localization and activity against a range of ion channels. We have also explored whether the degree of solvent exposure of the functional dyad, and the way that exposure changes over the course of MD simulations, might be informative in predicting the ability of ShKT family peptides to block K_V1.x channels.

The highest abundance of ShKT-Ts1 peptide was found in mesenterial filaments, a morphological structure that has a functional role in prey killing and digestion.[32] Several other peptides found in the milked venom of *Actinia tenebrosa* and *T. stephensoni* have similar tissue localization patterns to ShKT-Ts1, but their molecular targets remain uncharacterized.

Fully oxidized ShKT-Ts1 was obtained by cytoplasmic expression of a Trx fusion protein, from which it was cleaved using TEV. ShKT-Ts1 adopted the canonical disulfide connectivity pattern (C1—C6, C2—C4, and C3—C5) found in other ShKT peptides[18,24,25,28,29] (Figure 2B), and the Asp/Asn interaction with Lys–Thr, which is conserved among ShKT domains and has been shown to be important for peptide folding,[29,70] was also present. The surface representation of ShKT-Ts1 shows that, like other disulfide-rich peptides, ShKT-Ts1 lacks a canonical hydrophobic core, with the only hydrophobic residue buried being Phe24 (Figure 2C). All other hydrophobic side chains are solvent exposed or partially exposed.

While ShK has two short α-helices encompassing residues 14–19 and 21–24,[29] ShKT-Ts1 has a short 3_{10} helix (18–20) between two α-helices encompassing residues 8–14 and 22–27. The functional dyad Lys–Tyr found in ShK is present as Lys–Phe in ShKT-Ts1, suggesting that it may show activity against voltage-gated potassium channels, but our electrophysiology assays showed that ShKT-Ts1 has no activity against a range of voltage-gated and Ca^{2+}-activated ion channels (Figure S9). This demonstrates that prediction of the activity of ShKT peptides cannot be based solely on the amino acid sequence, and that other factors have to be considered.

DALI[54] was used to identify peptides structurally related to ShKT-Ts1; of the four structures identified, three have the functional dyad Lys–Tyr (ShK, BgK, and OspTx2a-p1) but only two (ShK and BgK) have been shown to block K_V1.3 with pM-nM potency. OspTx2a-p1 blocks K_V1.2 and K_V1.6 channel currents at low μM concentrations.[24] The ShKT domain of MMP23, which is not from a sea anemone, contains a dyad composed of Arg–Leu but still shows weak activity against K_V1.3 (~3 μM). Using MD simulations and PCA analysis, we found that the extent of solvent exposure of the dyad residues, and the effect thereon of conformational dynamics, may play a role in the ability of these peptides to block potassium channels. Our MD simulations showed that ShKT-Ts1 displays conformational dynamics around the 3_{10} helix (Figure 4); there is a rearrangement of this 3_{10} helix, which consequently shows a high root-mean-square fluctuation for the region Arg15–Lys23 (Figure 4A). PCA analysis show that the region comprising the 3_{10} helix is involved in conformational changes, where the region from Arg15 to Lys23 experiences changes in secondary structure, leading to an untwisted conformation that brings the side chains of Glu26 Oε and Arg14 Nη close to one another (4 Å; Figure 4C). These salt bridges probably stabilize the structure of ShKT-Ts1 but they also shield Phe24 from solvent (Figure 4C).

BgK and MMP23 also have solvent-exposed dyads. However, in MMP23 the dyad is not Lys–Tyr, but rather Arg-Leu, which may contribute to its low potency against K_V1.3.[18] OspTx2a-p1 has a very similar fold to BgK, but shows a low μM affinity against K_V1.2 and rK_V1.6. The dyad in this peptide is partially exposed, but Tyr25 is in a pocket that is completely buried when conformational changes during MD simulations bring Arg15 close to Lys24 (probably involving a local rearrangement of water).

These findings suggest a relationship between the extent of solvent exposure of the dyad, peptide dynamics, and activity against K_V1.x channels. Peptides with the dyad exposed can readily be recognized by the target and bind to the pore-vestibule region of the channel, but those with a buried dyad that does not become exposed during MD simulations, or with a partially exposed dyad that becomes buried during MD simulations may not show activity. Thus, advances in the accuracy of structure prediction, as exemplified by AlphaFold,[36] combined with MD simulations, offer a means to predict whether new sequences belonging to the ShKT family might show activity as K_V1.x channel blockers, or whether other potential targets should be explored. However, in the case of ShK-Ts1, the experimentally determined solution structure proved to be a more accurate basis for predicting activity against K_V1 channels than the AlphaFold-predicted structure. Further comparisons of experimentally determined solution structures, AlphaFold-predicted structures, and activity against K_V1 channels for ShKT peptides will be informative in establishing the predictive value of these approaches.

AUTHOR CONTRIBUTIONS

Karoline Sanches: Writing—original draft; methodology; validation; visualization; data curation; formal analysis; investigation. **Lauren M. Ashwood:** Investigation; writing—review and editing; methodology; validation; visualization; formal analysis; data curation; writing—original draft. **Abisola Ave-Maria Olushola-Siedoks:** Investigation; methodology; validation; visualization; writing—review and editing; formal analysis; data curation. **Dorothy C. C. Wai:** Investigation; methodology; validation; visualization; writing—review and editing; formal analysis; data curation. **Arfatur Rahman:** Investigation; methodology; validation; visualization; writing—review and editing; formal analysis; data curation. **Kashmala Shakeel:** Investigation; methodology; validation; visualization; formal analysis; data curation. **Muhammad Umair Naseem:** Investigation; methodology; validation; visualization; writing—review and editing; formal analysis; data curation. **Gyorgy Panyi:** Investigation; funding acquisition; methodology; validation; visualization; writing—review and editing; formal analysis; supervision; resources. **Peter J. Prentis:** Investigation; funding acquisition; methodology; validation; visualization; writing—review and editing; project administration; supervision; resources. **Raymond S. Norton:** Conceptualization; investigation; funding acquisition; writing—original draft; writing—review and editing; project administration; supervision; resources; visualization; validation.

ACKNOWLEDGMENTS

We would like to thank Brett Hamilton for his expert advice and assistance with the mass spectrometry imaging. Open access publishing facilitated by Monash University, as part of the Wiley - Monash University agreement via the Council of Australian University Librarians.

FUNDING INFORMATION

This work was funded in part by the Australian Research Council Centre for Fragment-Based Design (IC180100021 to Karoline Sanches and Raymond S. Norton) and the Hungarian National Research, Development and Innovation Office (K143071 to Gyorgy Panyi). This work was also supported by the Stipendium Hungaricum Scholarships from the Tempus Public Foundation (to Muhammad Umair Naseem) and the Richter Gedeon Talentum Foundation (to Kashmala Shakeel).

DATA AVAILABILITY STATEMENT

The data that support the findings of this study are openly available in Protein Data Bank at https://www.rcsb.org/, reference number 8SED, and BioMagResBank at https://www.bmrb.io, reference number 51896.

ORCID

Raymond S. Norton https://orcid.org/0000-0001-8893-0584

REFERENCES

1. Béress L. Biologically active compounds from coelenterates. *Pure Appl Chem*. 1982;54:1981-1994.
2. Honma T, Shiomi K. Peptide toxins in sea anemones: structural and functional aspects. *Marine Biotechnol*. 2006;8:1-10.
3. Norton RS. Sea anemone venom peptides. In: Kastin AJ, ed. *Handbook of Biologically Active Peptides*. Elsevier (Academic); 2013:430-436.
4. Prentis PJ, Pavasovic A, Norton RS. Sea anemones: quiet achievers in the field of peptide toxins. *Toxins (Basel)*. 2018;10:36.
5. Mitchell ML, Hamilton BR, Madio B, et al. The use of imaging mass spectrometry to study peptide toxin distribution in australian sea anemones. *Aust J Chem*. 2017;70:1235-1237.
6. Madio B, King GF, Undheim EAB. Sea anemone toxins: a structural overview. *Mar Drugs*. 2019;17:325.
7. Fu J, Liao Y, Jin AH, Gao B. Discovery of novel peptide neurotoxins from sea anemone species. *Front Biosci*. 2021;26:1256-1273.
8. Ashwood LM, Elnahriry KA, Stewart ZK, et al. Genomic, functional and structural analyses elucidate evolutionary innovation within the sea anemone 8 toxin family. *BMC Biol*. 2023;21:121.
9. Castañeda O, Sotolongo V, Amor AM, et al. Characterization of a potassium channel toxin from the Caribbean Sea anemone *Stichodactyla helianthus*. *Toxicon*. 1995;33:603-613.
10. Kalman K, Pennington MW, Lanigan MD, et al. ShK-Dap22, a potent Kv1.3-specific immunosuppressive polypeptide. *J Biol Chem*. 1998;273:32697-32707.
11. Chi V, Pennington MW, Norton RS, et al. Development of a sea anemone toxin as an immunomodulator for therapy of autoimmune diseases. *Toxicon*. 2012;59:529-546.
12. Tajti G, Wai DCC, Panyi G, Norton RS. The voltage-gated potassium channel $K_V1.3$ as a therapeutic target for venom-derived peptides. *Biochem Pharmacol*. 2020;181:114146.
13. Chang SC, Huq R, Chhabra S, et al. N-terminally extended analogues of the K^+ channel toxin from *Stichodactyla helianthus* as potent and selective blockers of the voltage-gated potassium channel Kv1.3. *FEBS J*. 2015;282:2247-2259.
14. Pennington MW, Beeton C, Galea CA, et al. Engineering a stable and selective peptide blocker of the Kv1.3 channel in T lymphocytes. *Mol Pharmacol*. 2009;75:762-773.
15. Pennington MW, Chang SC, Chauhan S, et al. Development of highly selective $K_V1.3$-blocking peptides based on the sea anemone peptide ShK. *Mar Drugs*. 2015;13:529-542.
16. Pennington MW, Rashid MH, Tajhya RB, Beeton C, Kuyucak S, Norton RS. A C-terminally amidated analogue of ShK is a potent and selective blocker of the voltage-gated potassium channel Kv1.3. *FEBS Lett*. 2012;586:3996-4001.
17. Tarcha EJ, Olsen CM, Probst P, et al. Safety and pharmacodynamics of dalazatide, a Kv1.3 channel inhibitor, in the treatment of plaque psoriasis: a randomized phase 1b trial. *PLoS One*. 2017;12:e0180762.
18. Rangaraju S, Khoo KK, Feng ZP, et al. Potassium channel modulation by a toxin domain in matrix metalloprotease 23. *J Biol Chem*. 2010;285:9124-9136.
19. Chhabra S, Chang SC, Nguyen HM, et al. Kv1.3 channel-blocking immunomodulatory peptides from parasitic worms: implications for autoimmune diseases. *FASEB J*. 2014;28:3952-3964.
20. UniProt Consortium. UniProt: the universal protein knowledgebase in 2023. *Nucleic Acids Res*. 2023;51:D523-D531.
21. Letunic I, Khedkar S, Bork P. SMART: recent updates, new developments and status in 2020. *Nucleic Acids Res*. 2021;49:D458-D460.
22. Shafee T, Mitchell ML, Norton RS. Mapping the chemical and sequence space of the ShKT superfamily. *Toxicon*. 2019;165:95-102.
23. Galea CA, Nguyen HM, George Chandy K, Smith BJ, Norton RS. Domain structure and function of matrix metalloprotease 23 (MMP23): role in potassium channel trafficking. *Cell Mol Life Sci*. 2014;71:1191-1210.
24. Sunanda P, Krishnarjuna B, Peigneur S, et al. Identification, chemical synthesis, structure, and function of a new K_V1 channel blocking peptide from *Oulactis* sp. *Pept Sci*. 2018;110:e24073.
25. Dauplais M, Lecoq A, Song J, et al. On the convergent evolution of animal toxins. Conservation of a diad of functional residues in potassium channel-blocking toxins with unrelated structures. *J Biol Chem*. 1997;272:4302-4309.
26. Gendeh GS, Young LC, de Medeiros CL, Jeyaseelan K, Harvey AL, Chung MC. A new potassium channel toxin from the sea anemone

Heteractis magnifica: isolation, cDNA cloning, and functional expression. *Biochemistry*. 1997;36:11461-11471.
27. Krishnarjuna B, MacRaild CA, Sunanda P, et al. Structure, folding and stability of a minimal homologue from *Anemonia sulcata* of the sea anemone potassium channel blocker ShK. *Peptides*. 2018;99:169-178.
28. Krishnarjuna B, Villegas-Moreno J, Mitchell ML, et al. Synthesis, folding, structure and activity of a predicted peptide from the sea anemone *Oulactis* sp. with an ShKT fold. *Toxicon*. 2018;150:50-59.
29. Tudor JE, Pallaghy PK, Pennington MW, Norton RS. Solution structure of ShK toxin, a novel potassium channel inhibitor from a sea anemone. *Nat Struct Mol Biol*. 1996;3:317-320.
30. Sachkova MY, Landau M, Surm JM, et al. Toxin-like neuropeptides in the sea anemone *Nematostella* unravel recruitment from the nervous system to venom. *Proc Natl Acad Sci U S A*. 2020;117:27481-27492.
31. Mitchell ML, Tonkin-Hill GQ, Morales RAV, Purcell AW, Papenfuss AT, Norton RS. Tentacle transcriptomes of the speckled anemone (Actiniaria: Actiniidae: *Oulactis* sp.): venom-related components and their domain structure. *Mar Biotechnol (NY)*. 2020;22:207-219.
32. Ashwood LM, Norton RS, Undheim EAB, Hurwood DA, Prentis PJ. Characterising functional venom profiles of anthozoans and medusozoans within their ecological context. *Mar Drugs*. 2020;18:202.
33. Ashwood LM, Undheim EAB, Madio B, et al. Venoms for all occasions: the functional toxin profiles of different anatomical regions in sea anemones are related to their ecological function. *Mol Ecol*. 2022;31:866-883.
34. Delgado A, Benedict C, Macrander J, Daly M. Never, Ever Make an Enemy… Out of an anemone: transcriptomic comparison of clownfish hosting sea anemone venoms. *Mar Drugs*. 2022;20:730.
35. Mazzi Esquinca ME, Correa CN, Marques de Barros G, Montenegro H, Mantovani de Castro L. Multiomic approach for bioprospection: investigation of toxins and peptides of Brazilian sea anemone *Bunodosoma caissarum*. *Mar Drugs*. 2023;21:197.
36. Jumper J, Evans R, Pritzel A, et al. Highly accurate protein structure prediction with AlphaFold. *Nature*. 2021;596:583-589.
37. Sher I, Chang SC, Li Y, et al. Conformational flexibility in the binding surface of the potassium channel blocker ShK. *Chembiochem*. 2014;15:2402-2410.
38. Meirovitch E, Tchaicheeyan O, Sher I, Norton RS, Chill JH. Structural dynamics of the potassium channel blocker ShK: SRLS analysis of ^{15}N relaxation. *J Phys Chem B*. 2015;119:15130-15137.
39. Iwakawa N, Baxter NJ, Wai DCC, et al. Conformational exchange in the potassium channel blocker ShK. *Sci Rep*. 2019;9:19307.
40. Sanches K, Wai DCC, Norton RS. Conformational dynamics in peptide toxins: implications for receptor interactions and molecular design. *Toxicon*. 2021;201:127-140.
41. Sanches K, Prypoten V, Chandy KG, Chalmers DK, Norton RS. Interaction of the inhibitory peptides ShK and HmK with the voltage-gated Potassium Channel $K_V1.3$: role of conformational dynamics. *J Chem Inf Model*. 2023;63:3043-3053.
42. Wallace CC. Hexacorals 1: sea anemones and anemone-like animals (Actiniaria, Zoanthidea, Corallimorpharia, Ceriantharia and Antipatharia). In: Hutchings P, Kingsford M, Hoegh-Guldberg O, eds. *The Great Barrier Reef: Biology, Environment and Management*. CSIRO; 2008:198-207.
43. Surm JM, Smith HL, Madio B, et al. A process of convergent amplification and tissue-specific expression dominates the evolution of toxin and toxin-like genes in sea anemones. *Mol Ecol*. 2019;28:2272-2289.
44. Marley J, Lu M, Bracken C. A method for efficient isotopic labeling of recombinant proteins. *J Biomol NMR*. 2001;20:71-75.
45. Sattler M, Schleucher J, Griesinger C. Heteronuclear multidimensional NMR experiments for the structure determination of proteins in solution employing pulsed field gradients. *Prog Nucl Mag Res Spec*. 1999;34:93-158.
46. Hyberts SG, Milbradt AG, Wagner AB, Arthanari H, Wagner G. Application of iterative soft thresholding for fast reconstruction of NMR data non-uniformly sampled with multidimensional Poisson gap scheduling. *J Biomol NMR*. 2012;52:315-327.
47. Delaglio F, Grzesiek S, Vuister GW, Zhu G, Pfeifer J, Bax A. NMRPipe: a multidimensional spectral processing system based on UNIX pipes. *J Biomol NMR*. 1995;6:277-293.
48. Vranken WF, Boucher W, Stevens TJ, et al. The CCPN data model for NMR spectroscopy: development of a software pipeline. *Proteins*. 2005;59:687-696.
49. Maciejewski MW, Schuyler AD, Gryk MR, et al. NMRbox: a resource for biomolecular NMR computation. *Biophys J*. 2017;112:1529-1534.
50. Rieping W, Habeck M, Bardiaux B, Bernard A, Malliavin TE, Nilges M. ARIA2: automated NOE assignment and data integration in NMR structure calculation. *Bioinformatics*. 2007;23:381-382.
51. Linge JP, O'Donoghue SI, Nilges M. Automated assignment of ambiguous nuclear Overhauser effects with ARIA. *Methods Enzymol*. 2001;339:71-90.
52. Shen Y, Bax A. Protein backbone and sidechain torsion angles predicted from NMR chemical shifts using artificial neural networks. *J Biomol NMR*. 2013;56:227-241.
53. Bhattacharya A, Tejero R, Montelione GT. Evaluating protein structures determined by structural genomics consortia. *Proteins*. 2007;66:778-795.
54. Holm L. Using Dali for protein structure comparison. *Methods Mol Biol*. 2020;2112:29-42.
55. Abraham MJ, Murtola T, Schulz R, et al. GROMACS: high performance molecular simulations through multi-level parallelism from laptops to supercomputers. *SoftwareX*. 2015;1–2:19-25.
56. Hornak V, Abel R, Okur A, Strockbine B, Roitberg A, Simmerling C. Comparison of multiple Amber force fields and development of improved protein backbone parameters. *Proteins*. 2006;65:712-725.
57. Abascal JL, Vega C. A general purpose model for the condensed phases of water: TIP4P/2005. *J Chem Phys*. 2005;123:234505.
58. Bussi G, Zykova-Timan T, Parrinello M. Isothermal-isobaric molecular dynamics using stochastic velocity rescaling. *J Chem Phys*. 2009;130:074101.
59. Bussi G, Donadio D, Parrinello M. Canonical sampling through velocity rescaling. *J Chem Phys*. 2007;126:014101.
60. Vichai V, Kirtikara K. Sulforhodamine B colorimetric assay for cytotoxicity screening. *Nat Protoc*. 2006;1:1112-1116.
61. Rahman A, Matthews MA, Nowell CJ, et al. Enhanced nitric oxide production by macrophages treated with a cell-penetrating peptide conjugate. *Bioorg Chem*. 2022;123:105763.
62. Hamill OP, Marty A, Neher E, Sakmann B, Sigworth FJ. Improved patch-clamp techniques for high-resolution current recording from cells and cell-free membrane patches. *Pflugers Arch*. 1981;391:85-100.
63. Rezazadeh S, Kurata HT, Claydon TW, Kehl SJ, Fedida D. An activation gating switch in Kv1.2 is localized to a threonine residue in the S2-S3 linker. *Biophys J*. 2007;93:4173-4186.
64. Sievers F, Wilm A, Dineen D, et al. Fast, scalable generation of high-quality protein multiple sequence alignments using Clustal omega. *Mol Syst Biol*. 2011;7:539.
65. Waterhouse AM, Procter JB, Martin DM, Clamp M, Barton GJ. Jalview version 2—a multiple sequence alignment editor and analysis workbench. *Bioinformatics*. 2009;25:1189-1191.
66. Bolyen E, Rideout JR, Dillon MR, et al. Reproducible, interactive, scalable and extensible microbiome data science using QIIME 2. *Nat Biotechnol*. 2019;37:852-857.
67. Wang B, Kennedy MA. Principal components analysis of protein sequence clusters. *J Struct Funct Genomics*. 2014;15:1-11.
68. Vazquez-Baeza Y, Pirrung M, Gonzalez A, Knight R. EMPeror: a tool for visualizing high-throughput microbial community data. *Gigascience*. 2013;2:16.
69. Hoch JC, Baskaran K, Burr H, et al. Biological Magnetic Resonance Data Bank. *Nucleic Acids Res*. 2023;51:D368-D376.